Supporting Information

Successive redox modulation in an iron(II) spin-crossover framework

Bang-Heng Lyu,[a] Ze-Yu Ruan,[a] Wen Cui,[a] Si-Guo Wu,[a]* Zhao-Ping Ni[a]* and Ming-Liang Tong[a]*

Key Laboratory of Bioinorganic and Synthetic Chemistry of Ministry of Education, School of Chemistry, Sun Yat-Sen University, Guangzhou, 510275, P. R. China

Contents

Thermogravimetric analysis

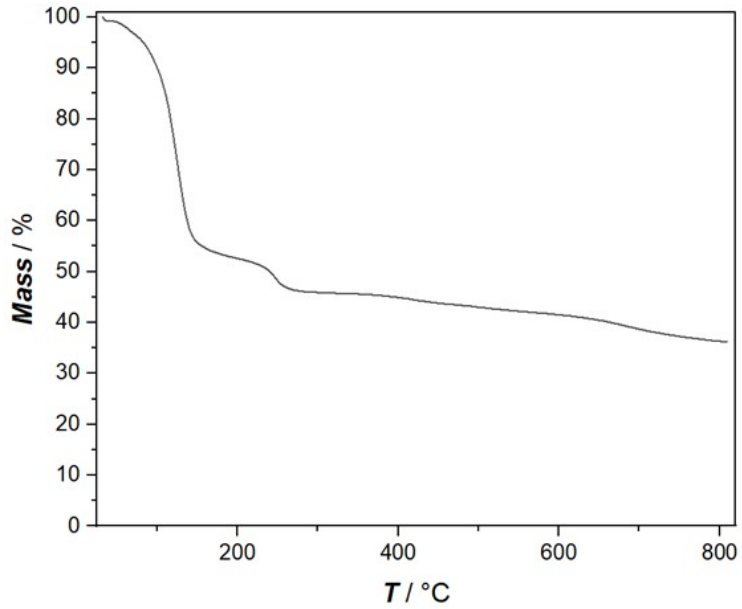

Figure S1. Thermogravimetric analysis curve of **1**. The weight loss of 53.4% is close to the theoretical value of 53.0% corresponding to the escape of 2 H_2O and 7 TCE molecules.

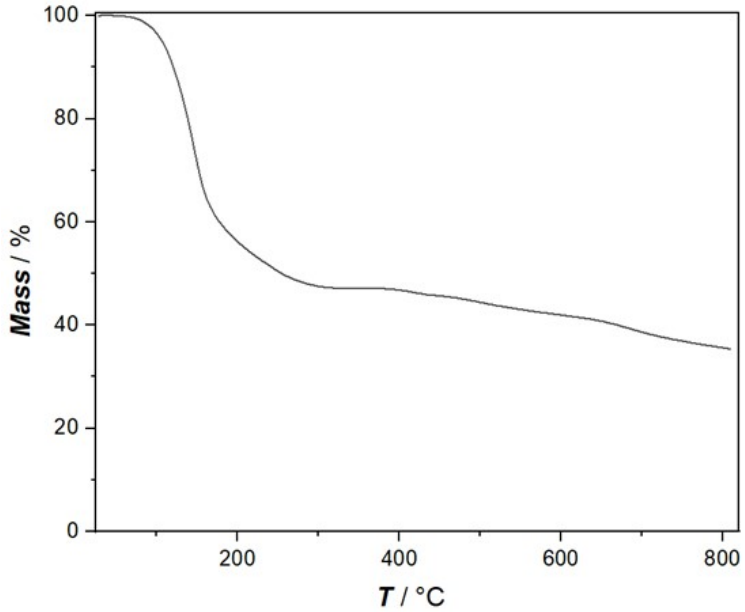

Figure S2. Thermogravimetric analysis curve of **2**. The weight loss of 52.6% is close to the theoretical value of 51.9% corresponding to the escape of 1 I_2 and 7 TCE molecules.

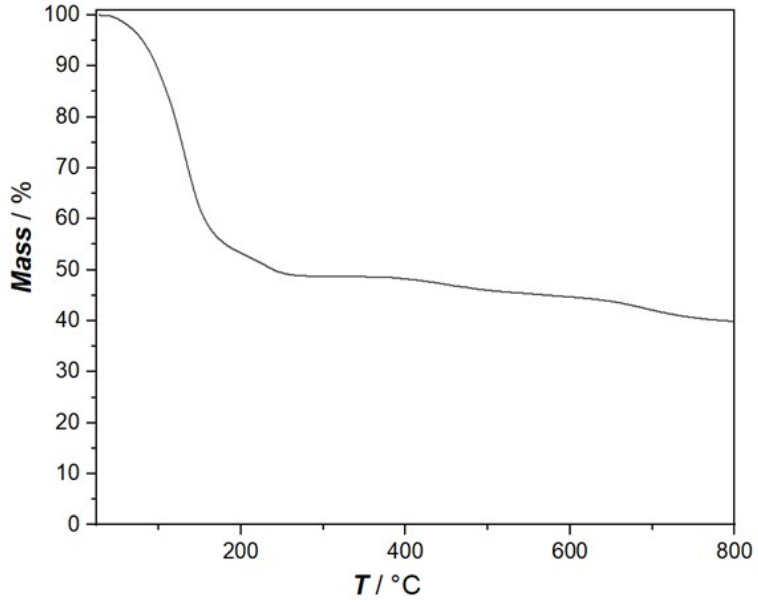

Figure S3. Thermogravimetric analysis curve of **3**. The weight loss of 51.1% is close to the theoretical value of 50.3% corresponding to the escape of 1 H_2O and 8 TCE molecules.

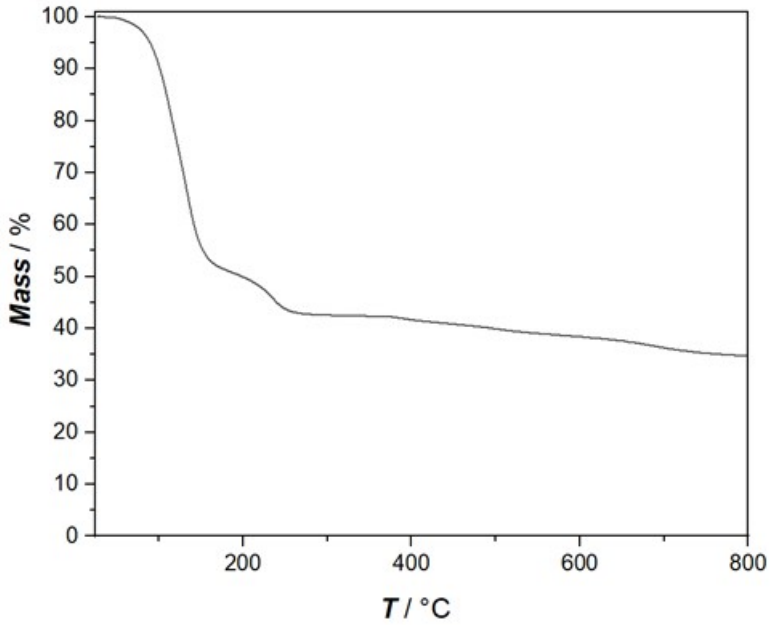

Figure S4. Thermogravimetric analysis curve of **4**. The weight loss of 57.2% is close to the theoretical value of 57.7% corresponding to the escape of 3 H_2O and 8 TCE molecules.

Crystal data

Table S1. Crystallographic data for **1**.

Empirical formula	$C_{62}H_{50}AuCl_{28}O_2FeIN_6$	
Formula weight	2283.39	
Temperature/K	300.00	120.00
Crystal system	orthorhombic	orthorhombic
Space group	*Pmmm*	*Pmmm*
a / Å	10.5117(10)	10.0549(7)
b / Å	14.7107(14)	14.5520(10)
c / Å	16.9860(17)	16.5361(12)
α / °	90	90
β / °	90	90
γ / °	90	90
Volume / Å^3	2626.6(4)	2419.5(3)
Z	1	1
ρ_{calc} g/cm^3	1.444	1.567
μ/mm^{-1}	2.575	2.795
F(000)	1114.0	1114.0
Crystal size / mm^3	0.226 × 0.215 × 0.205	0.226 × 0.215 × 0.205
Reflections collected	24957	36892
Independent reflections	3532	3383
Goodness-of-fit on F^2	1.081	1.185
Final *R* indexes [$I>=2\sigma(I)$]	R_1 = 0.0829, wR_2 = 0.2287	R_1 = 0.0519, wR_2 = 0.1533
Final *R* indexes [all data]	R_1 = 0.0882, wR_2 = 0.2337	R_1 = 0.0539, wR_2 = 0.1556
Largest diff. peak/hole / e Å^{-3}	3.57/−1.28	2.52/−0.96
CCDC	2249183	2249182

[a] $R_1 = \Sigma||F_o| - |F_c||/\Sigma|F_o|$; [b] $wR_2 = \{[\Sigma w(F_o^2-F_c^2)^2]/\Sigma[w(F_o^2)^2]\}^{1/2}$

Table S2. Crystallographic data for **2**.

Empirical formula	$C_{62}H_{46}AuCl_{28}FeI_5N_6$	
Formula weight	2754.96	
Temperature/K	320.0	102.00
Crystal system	orthorhombic	orthorhombic
Space group	*Pmmm*	*Fmmm*
a / Å	10.4944(9)	19.9965(11)
b / Å	14.6760(13)	28.2630(17)
c / Å	17.0345(15)	33.579(2)
α / °	90	90
β / °	90	90
γ / °	90	90
Volume / Å^3	2623.6(4)	18977.4(19)
Z	1	8
ρ_{calc} g/cm^3	1.744	1.928
μ/mm^{-1}	3.754	4.152
F(000)	1306.0	10448.0
Crystal size / mm^3	0.397 × 0.346 × 0.279	0.234 × 0.217 × 0.186
Reflections collected	23389	44070
Independent reflections	3085	6286
Goodness-of-fit on F^2	1.120	1.066
Final *R* indexes [$I>=2\sigma(I)$]	$R_1 = 0.1028$, $wR_2 = 0.2803$	$R_1 = 0.0869$, $wR_2 = 0.2724$
Final *R* indexes [all data]	$R_1 = 0.1059$, $wR_2 = 0.2843$	$R_1 = 0.1082$, $wR_2 = 0.2919$
Largest diff. peak/hole / e Å^{-3}	3.75/−2.17	2.85/−3.67
CCDC	2249191	2249190

[a] $R_1 = \Sigma||F_o| - |F_c||/\Sigma|F_o|$; [b] $wR_2 = \{[\Sigma w(F_o^2-F_c^2)^2]/\Sigma[w(F_o^2)^2]\}^{1/2}$

Table S3. Crystallographic data for **3**.

Empirical formula	$C_{64}H_{50}AuCl_{32}OBr_5FeN_6$
Formula weight	2705.86
Temperature/K	120.0
Crystal system	orthorhombic
Space group	*Pmmm*
a / Å	10.006(3)
b / Å	14.398(5)
c / Å	16.704(5)
α / °	90
β / °	90
γ / °	90
Volume / Å^3	2406.5(13)
Z	1
ρ_{calc} g/cm^3	1.867
μ/mm^{-1}	4.679
F(000)	1308.0
Crystal size / mm^3	0.143 × 0.121 × 0.116
Reflections collected	24481
Independent reflections	2257
Goodness-of-fit on F^2	1.024
Final *R* indexes [$I>=2\sigma(I)$]	R_1 = 0.0923, wR_2 = 0.2550
Final *R* indexes [all data]	R_1 = 0.1326, wR_2 = 0.2826
Largest diff. peak/hole / e Å^{-3}	2.78/−1.21
CCDC	2249194

[a] $R_1 = \Sigma||F_o| - |F_c||/\Sigma|F_o|$; [b] $wR_2 = \{[\Sigma w(F_o^2-F_c^2)^2]/\Sigma[w(F_o^2)^2]\}^{1/2}$

Table S4. Selected bond lengths for **1**

T / K	300	120
Fe1−N1 / Å	2.124(9)	1.906(6)
Fe1−N2 / Å	2.235(5)	2.002(3)
<Fe−N>[a] / Å	2.198	1.970
ΣFe[b] / °	4.78	4.19
Au1−C1	1.958(10)	1.964(7)
∠Fe1−N1−C1 / °	180	180
∠Au1−C1−N1 / °	180	180

[a]average Fe−N bond length; [b]Octahedral distortion parameters.

Table S5. Selected bond lengths for **2**

T / K	320	102
Fe1−N1 / Å	2.143(13)	1.892(10)
Fe1−N2 / Å	2.227(9)	1.997(6)
<Fe−N>[a] / Å	2.199	1.962
ΣFe[b] / °	3.58	14.5
Au1−C1	1.949(14)	1.943(12)
Au1−I1	2.699(11)	2.617(3)
Au1−I1A	2.658(14)	2.607(5)
Au1−I1B	-	2.586(9)
∠Fe1−N1−C1 / °	180	180
∠Au1−C1−N1 / °	180	180

[a]average Fe−N bond length; [b]Octahedral distortion parameters.

Table S6. Selected bond lengths for **3**

T / K	120
Fe1−N1 / Å	1.86(2)
Fe1−N2 / Å	2.055(12)
<Fe−N>[a] / Å	1.990
ΣFe[b] / °	10.6
Au1−C1	1.96(3)
Au1−Br1	2.405(9)
Au1−Br2	2.405(13)
Au1−Br2A	2.394(12)
∠Fe1−N1−C1 / °	180
∠Au1−C1−N1 / °	180

[a]average Fe−N bond length; [b]Octahedral distortion parameters.

Powder X-Ray Diffraction

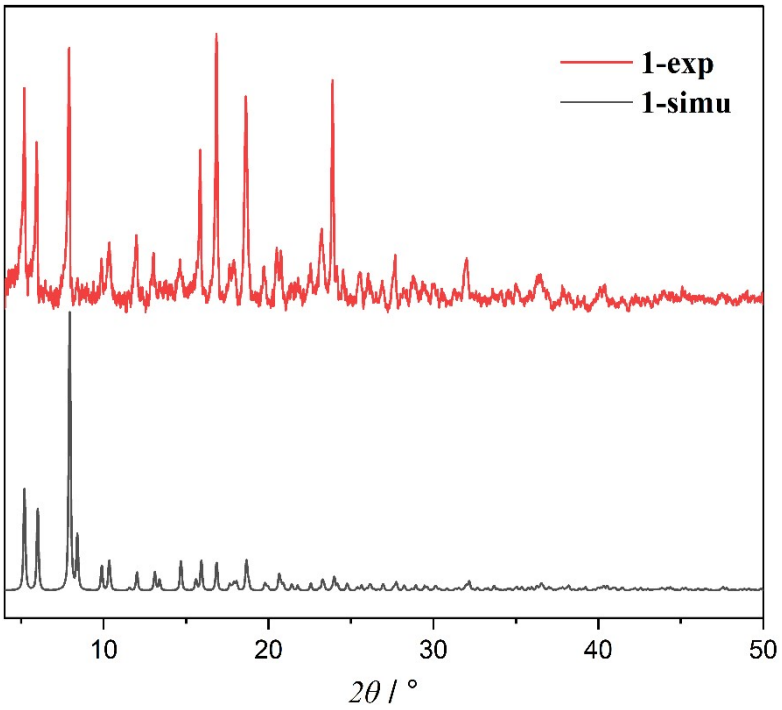

Figure S5. Powder X-ray diffraction (PXRD) patterns for **1**. The simulated PXRD pattern was obtained from crystal data at 300 K.

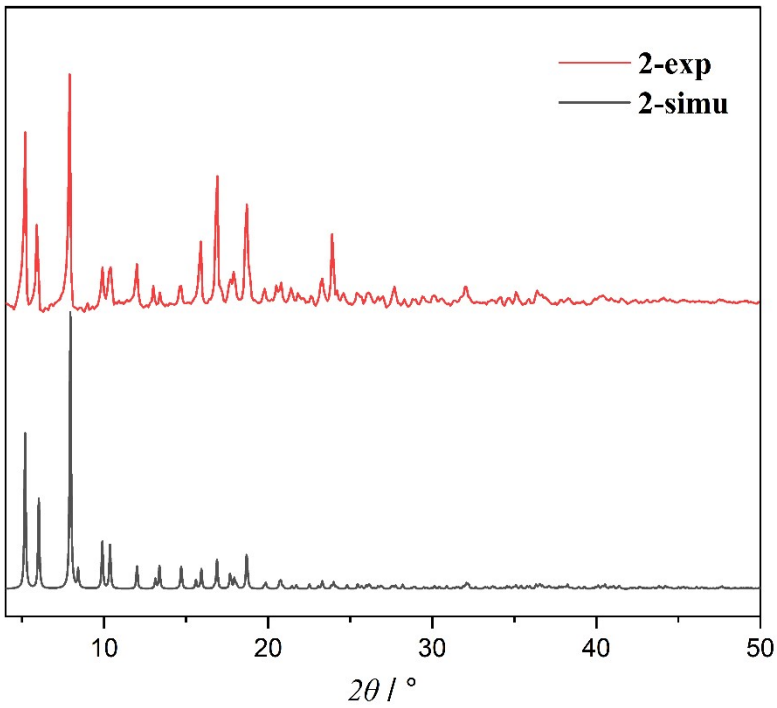

Figure S6. Powder X-ray diffraction (PXRD) patterns for **2**. The simulated PXRD pattern was obtained from crystal data at 320 K.

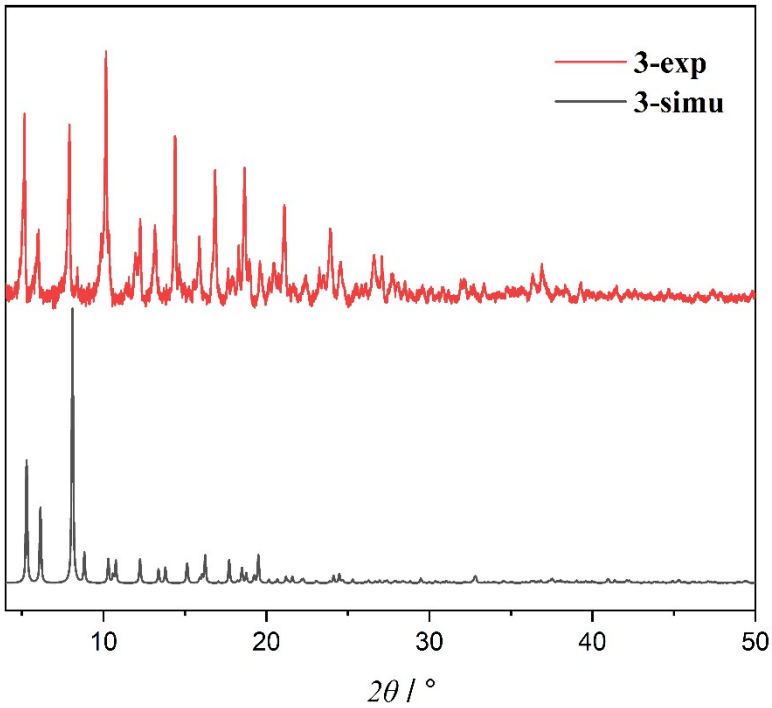

Figure S7. Powder X-ray diffraction (PXRD) patterns for **3**. The simulated PXRD pattern was obtained from crystal data at 120 K.

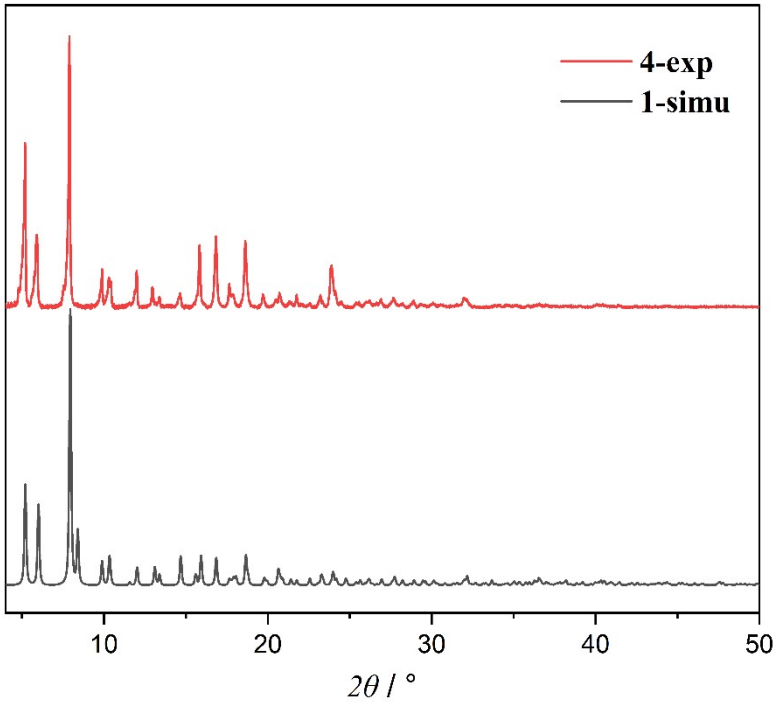

Figure S8. Powder X-ray diffraction (PXRD) patterns for **4**. The simulated PXRD pattern was obtained from crystal data of **1** at 300 K.

Infrared spectra

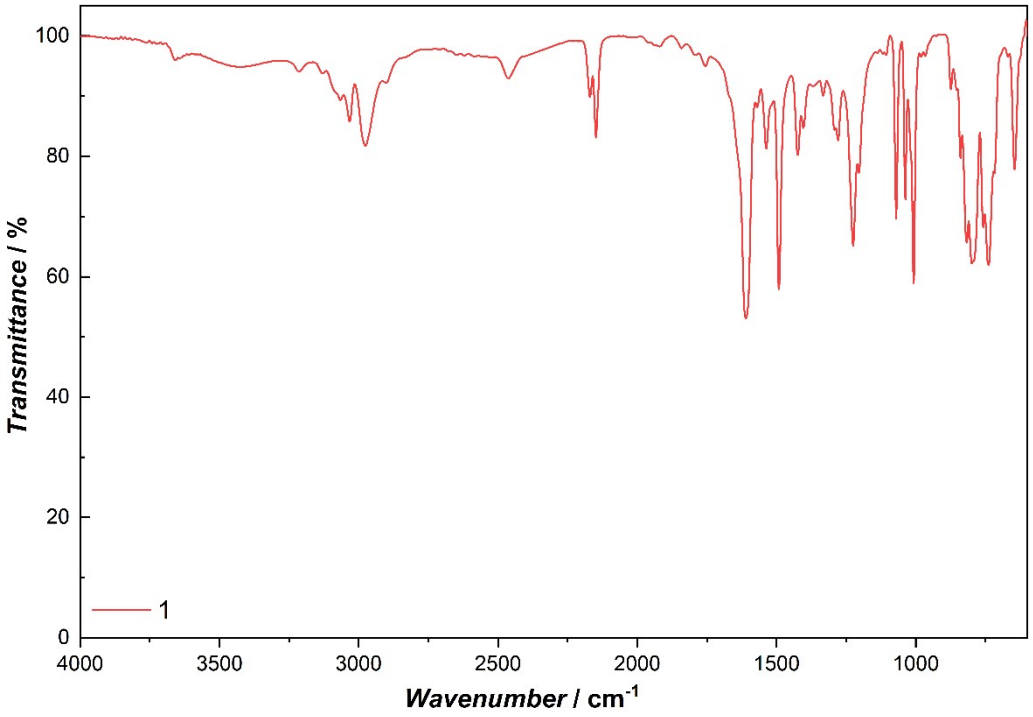

Figure S9. The infrared spectrum of **1**.

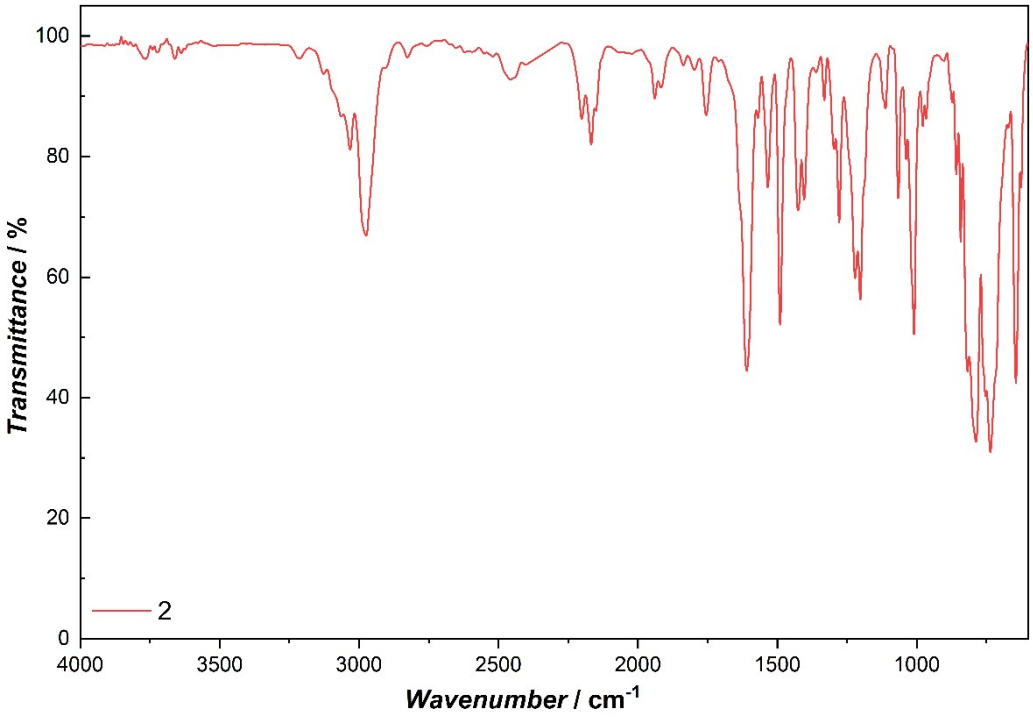

Figure S10. The infrared spectrum of **2**.

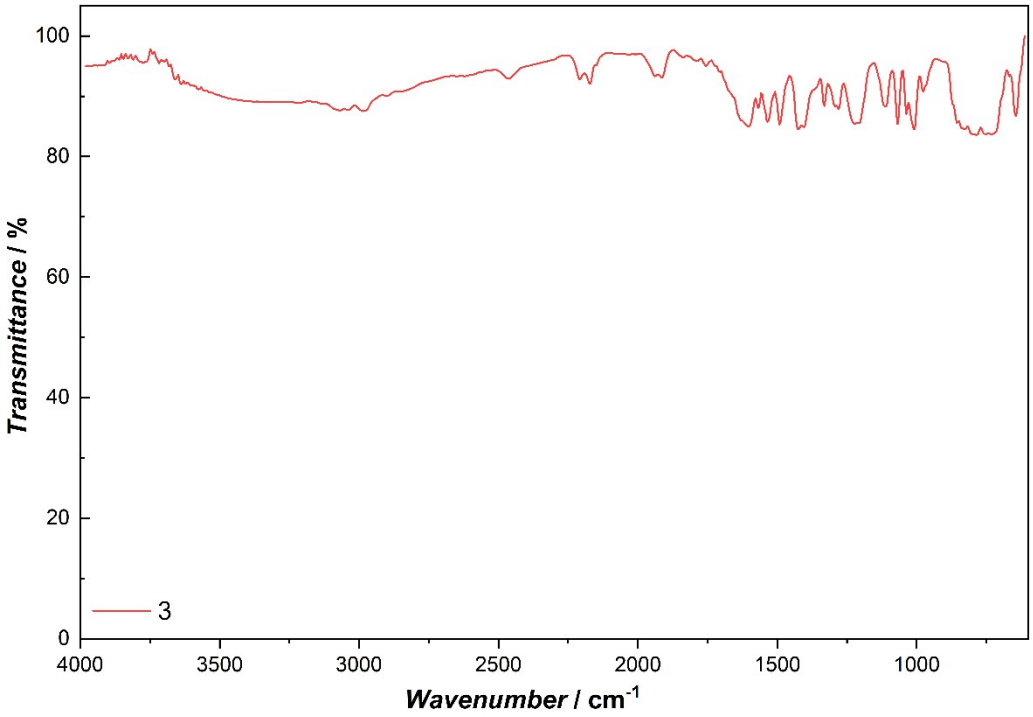

Figure S11. The infrared spectrum of **3**.

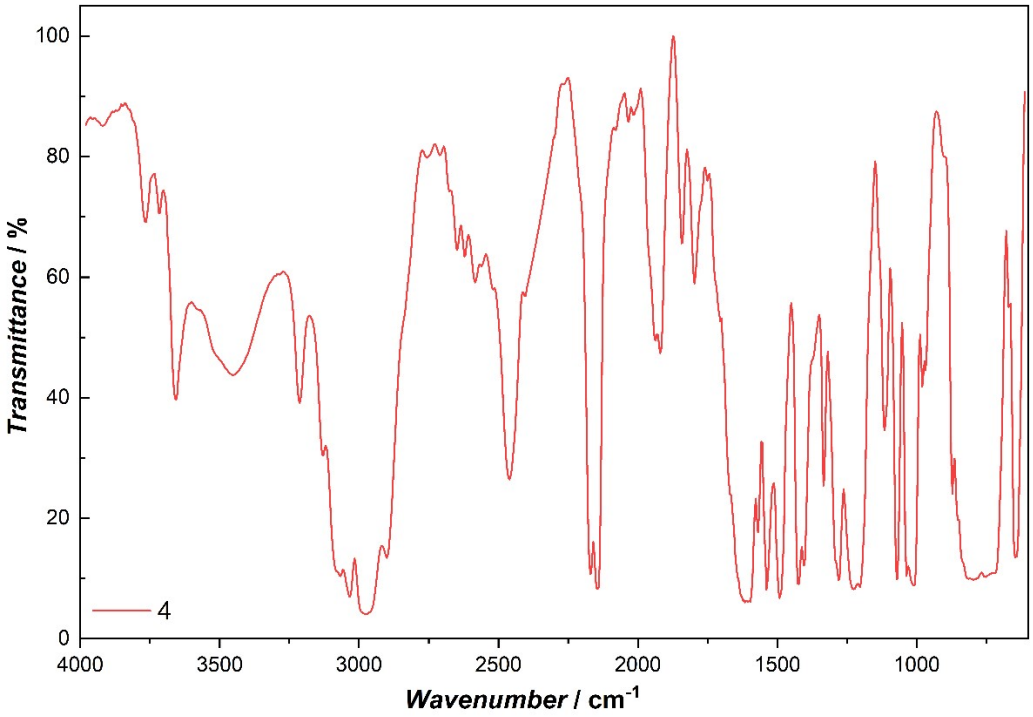

Figure S12. The infrared spectrum of **4**.

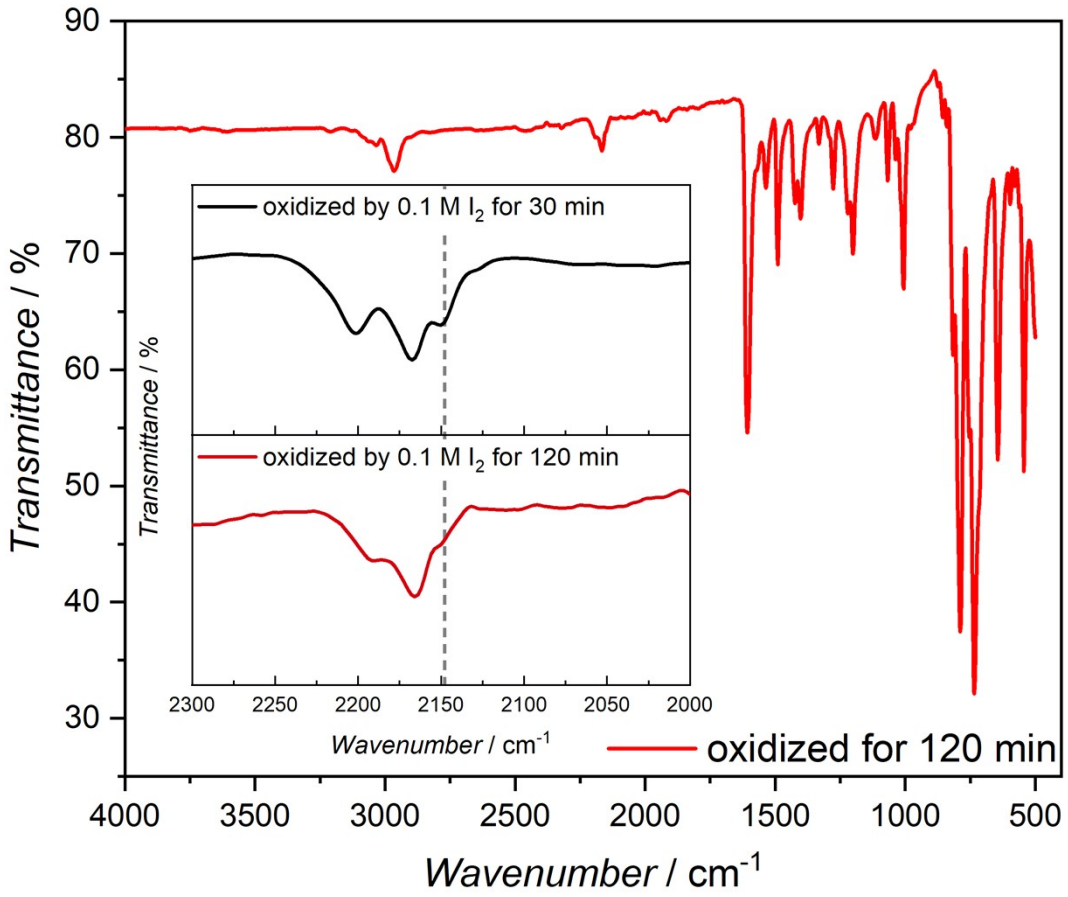

Figure S13. The infrared spectrum of the oxidation product obtained by reacting **1** with 0.1 M I_2 for 120 min. Inset: the enlarged view of the cyanide vibration signals for the products after being oxidized by 0.1 M I_2 for 30 and 120 min.

XPS Measurements

X-ray photoelectron spectroscopy (XPS) measurements were carried out with the Thermo Fisher Scientific ESCALAB Xi+ system (Al-K_α source). Sequential XPS spectra were recorded by scanning the electron analyzer from 100 to 75 eV (increment: 0.05 V, pass energy: 20.0 eV). The total acquisition times for Au 4f scan were about 3.5 min for **1**, about 0.5 min for **2** and **3** and about 1 min for **4**. The peak analysis processes were carried out with the XPSPEAK41 package. The electron-scattering background was deducted using a Shirley method without changing the intrinsic profile of raw data. The intervals and area ratios of $4f_{7/2}$ and $4f_{5/2}$ were restricted to 3.67 eV and 4:3 according to the literature. The full-width-at-half-maximum of the $4f_{7/2}$ and $4f_{5/2}$ doublets was fitted equally. The best fitted results were obtained by using a pseudo-Voigt function (20% Gaussian and 80% Lorentzien).

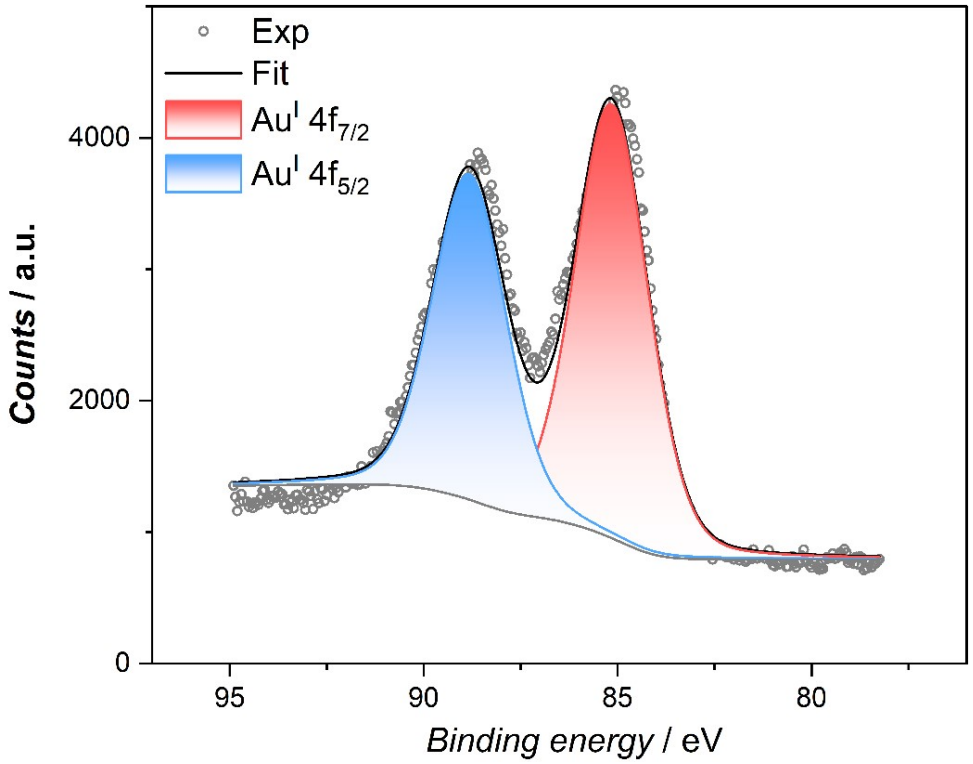

Figure S14. X-ray photoelectron spectroscopy of Au 4f in **1**.

Table S7. The parameters of best fit results of Au 4f in **1**.

Peak	Position / eV	Area	FWHM / eV
Au^I $4f_{7/2}$	85.154	8634.142	2.243
Au^I $4f_{5/2}$	88.824	6475.606	2.243

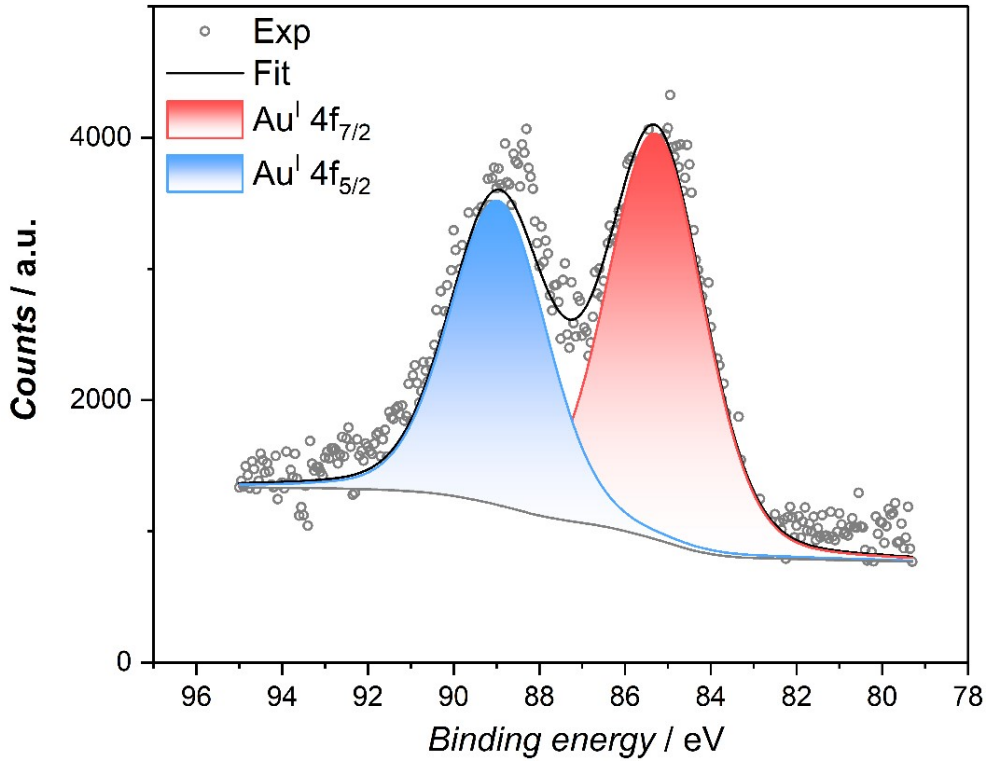

Figure S15. X-ray photoelectron spectroscopy of Au 4f in **2**.

Table S8. The parameters of best fit results of Au 4f in **2**.

Peak	Position / eV	Area	FWHM / eV
Au^{I} $4f_{7/2}$	85.287	9663.406	2.680
Au^{I} $4f_{5/2}$	88.957	7247.555	2.680

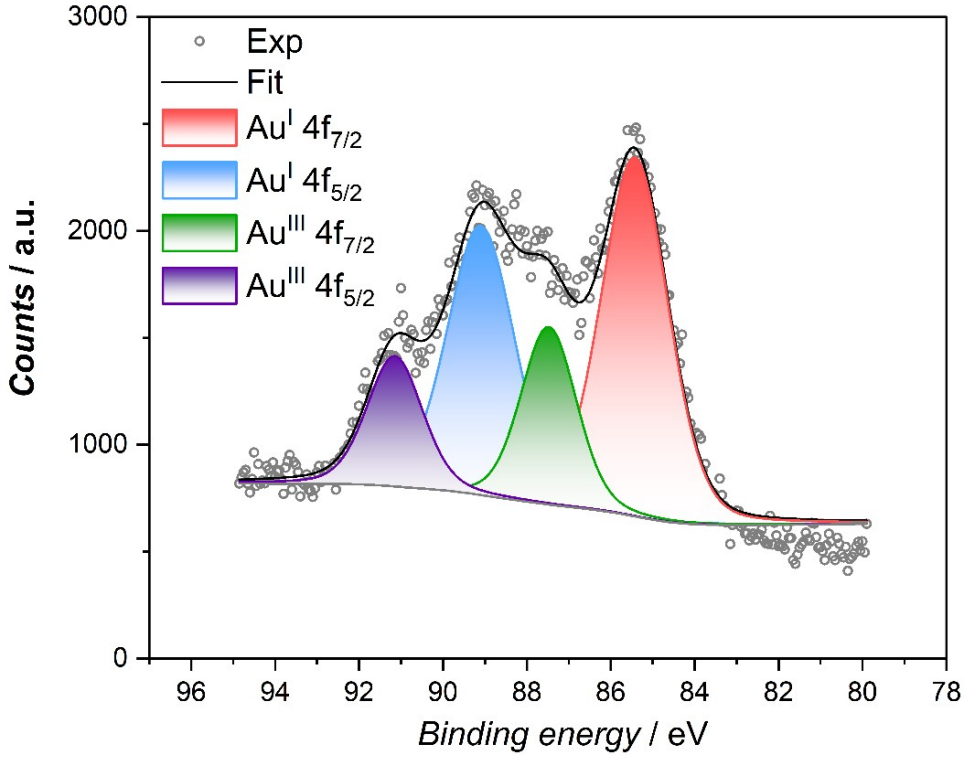

Figure S16. X-ray photoelectron spectroscopy of Au 4f in **3**.

Table S9. The parameters of best fit results of Au 4f in **3**.

Peak	Position / eV	Area	FWHM / eV
Au^{I} $4f_{7/2}$	85.427	3694.506	1.887
Au^{I} $4f_{5/2}$	89.097	2770.879	1.887
Au^{III} $4f_{7/2}$	87.479	1510.974	1.560
Au^{III} $4f_{5/2}$	91.149	1133.231	1.560

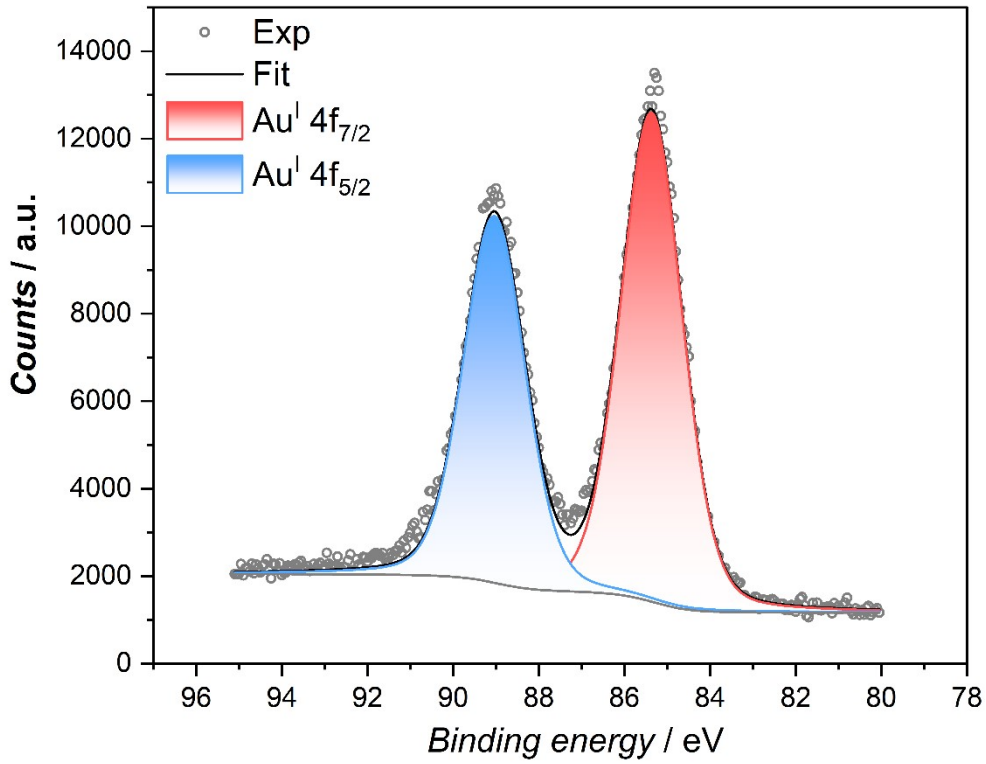

Figure S17. X-ray photoelectron spectroscopy of Au 4f in **4**.

Table S10. The parameters of best fit results of Au 4f in **4**.

Peak	Position / eV	Area	FWHM / eV
Au^{I} 4f$_{7/2}$	85.368	22125.31	1.697
Au^{I} 4f$_{5/2}$	89.038	16593.98	1.697

Magnetization measurements

Magnetic susceptibility measurements were performed on a Quantum Design PPMS3 SQUID magnetometer with a sweep rate of 2 K min^{-1} under applied field of 5 kOe. Polycrystalline samples were packed in plastic film with a small amount of mother liquor. Data were corrected for the signal of the sample holder and diamagnetic contribution calculated from Pascal's constants.

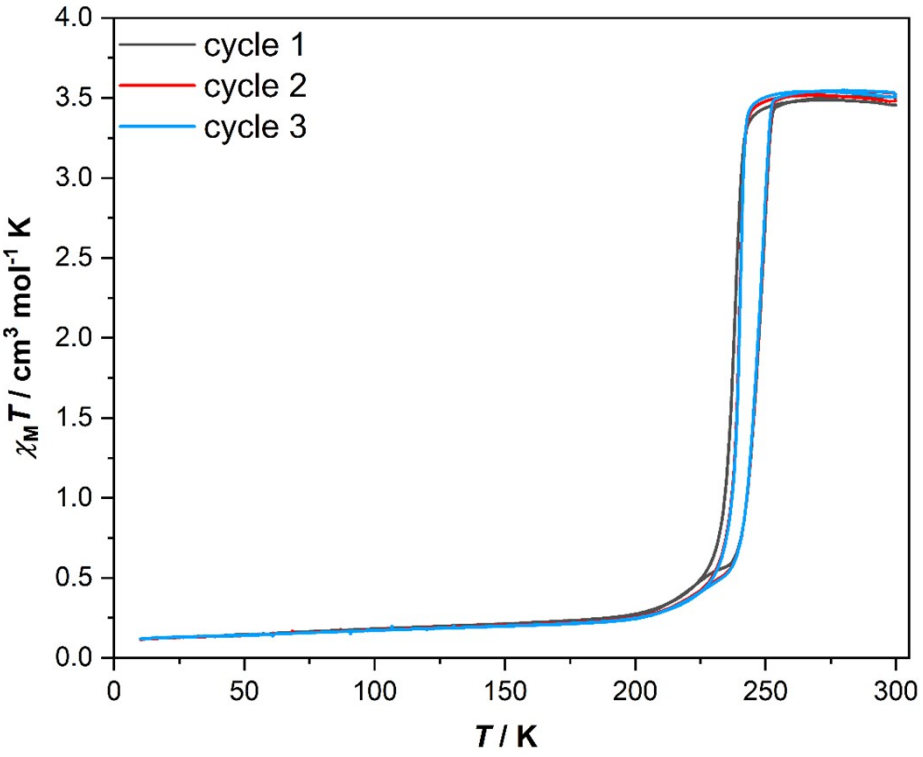

Figure S18. The temperature-dependent magnetic susceptibility data of **1** with a sweep rate of 2 K min^{-1}.

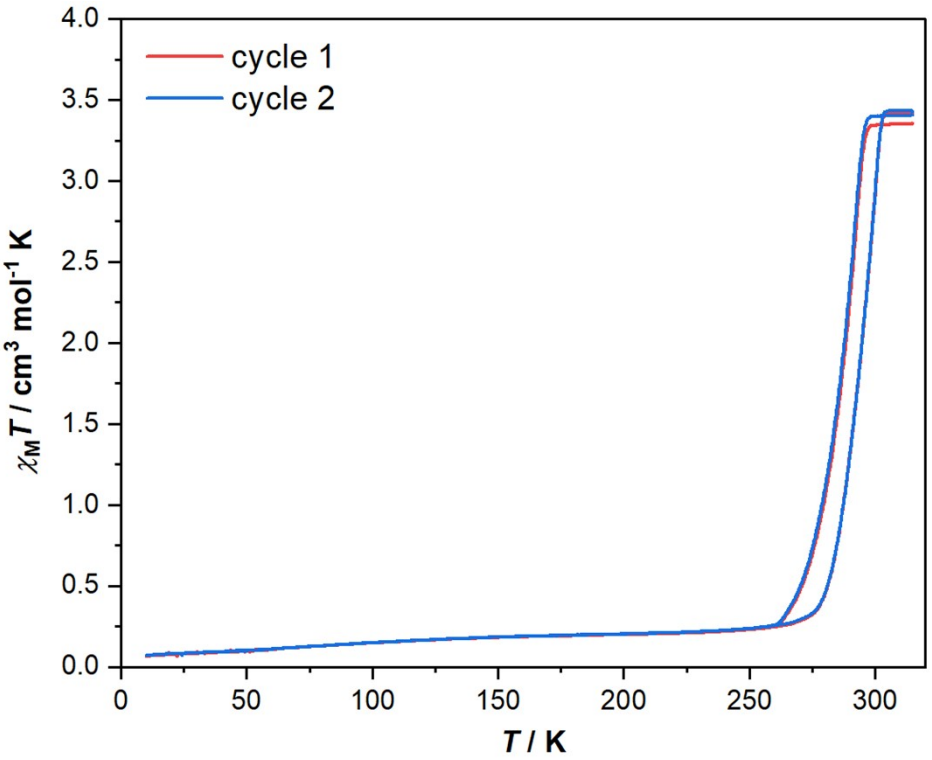

Figure S19. The temperature-dependent magnetic susceptibility data of **2** with a sweep rate of 2 K min^{-1}.

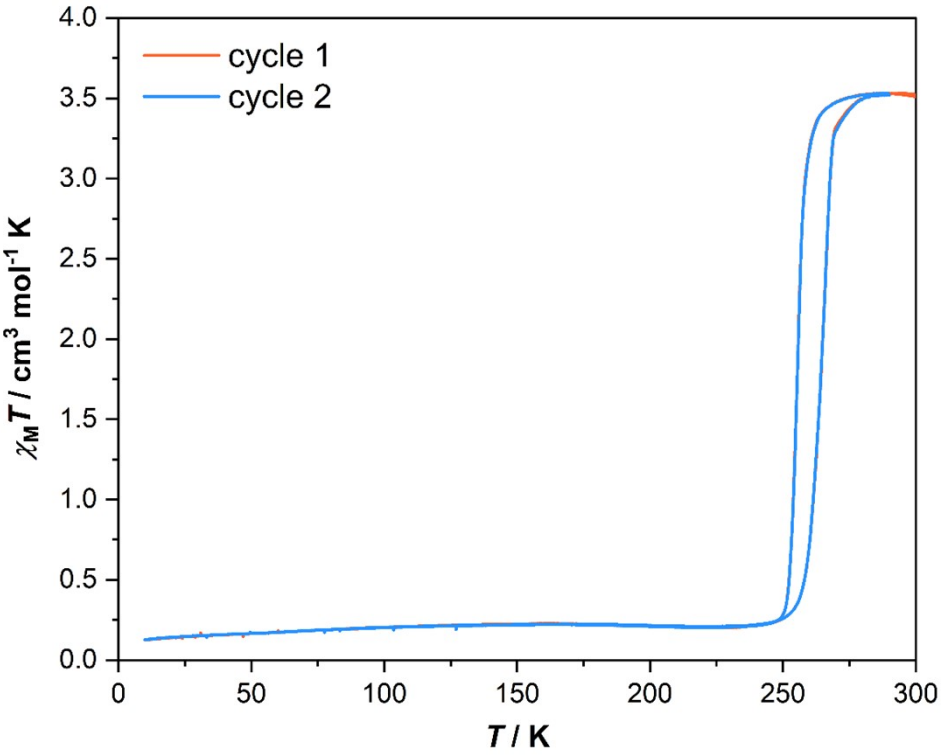

Figure S20. The temperature-dependent magnetic susceptibility data of **3** with a sweep rate of 2 K min^{-1}.

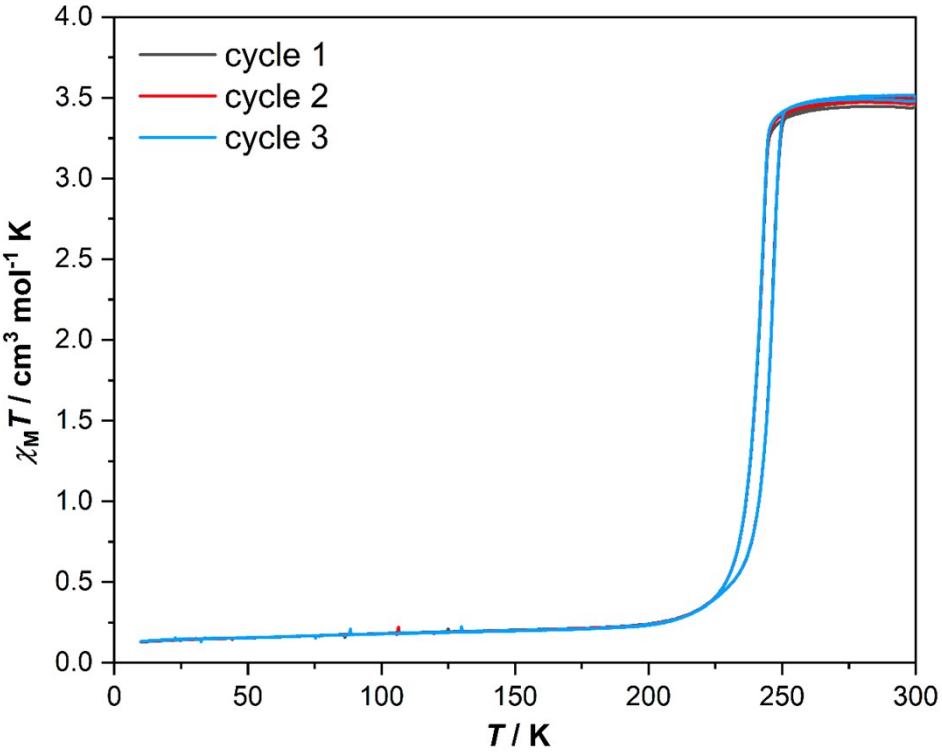

Figure S21. The temperature-dependent magnetic susceptibility data of **4** with a sweep rate of 2 K min^{-1}.